Article:
Xu, L., Braun, L.J., Rönnlund, D. et al. (2018) Nanoscale localization of proteins within focal adhesions indicates discrete functional assemblies with selective force-dependence. The FEBS Journal, 285 (9). pp. 1635-1652. ISSN: 1742-464X

https://doi.org/10.1111/febs.14433

Nanoscale localization of proteins within focal adhesions indicates discrete functional assemblies with selective force-dependence

Lei Xu[1], Laura J. Braun[2], Daniel Rönnlund[1], Jerker Widengren[1], Pontus Aspenström[2], Annica K. B. Gad[3]

1. Experimental Biomolecular Physics, Department of Applied Physics, KTH Royal Institute of Technology, AlbaNova University Center, 106 91 Stockholm, Sweden.
2. Department of Microbiology, Tumor and Cell Biology, Karolinska Institutet, Nobels v. 16, Box 280, 171 77 Stockholm, Sweden.
3. CQM – Centro de Químíca da Madeira, University of Madeira, Campus da Penteada, Funchal, Portugal.

Corresponding author: Annica Gad

Annica Gad

CQM – Centro de Químíca da Madeira, Universidade da Madeira, Campus da Penteada,

9020-105 Funchal

Portugal

Tel: +351-291-705254

E-mail: annica.gad@staff.uma.pt

Running title: Force dependency of nanoscale adhesions

List of defined abbreviations

STED	Stimulated emission depletion
FARPs	focal adhesion-related particles
FAs	focal adhesions
PALM	Photo-activated localization microscopy
dSTORM	Stochastic optical reconstruction microscopy
ICCS	Image cross correlation spectroscopy
ECM	Extracellular matrix

Key words: Quantitative imaging, Focal adhesions, Co-localization, Stimulated emission depletion (STED) microscopy, focal adhesion-related particles (FARPs).

Abstract

Focal adhesions are subcellular regions at the micrometer scale that link the cell to the surrounding microenvironment and control vital cell functions. However, the spatial architecture of focal adhesions remains unclear at the nanometer scale. We used two-color and three-color super-resolution stimulated emission depletion microscopy to determine the spatial distributions and co-localization of endogenous focal adhesion components in fibroblasts. Our data indicate that adhesion proteins inside, but not outside, focal adhesions are organized into nanometer size units of multi-protein assemblies. The loss of contractile force reduced the nanoscale co-localization between different types of proteins, while it increased this co-localization between markers of the same type. This suggests that actomyosin-dependent force exerts a non-random, specific, control of the localization of adhesion proteins within cell-matrix adhesions. These observations are consistent with the possibility that proteins in cell-matrix adhesions are assembled in nanoscale particles, and that force regulates the localization of the proteins therein in a protein-specific manner. This detailed knowledge of how the organization of focal adhesion components at the nanometer scale is linked to the capacity of the cells to generate contractile forces expands our understanding of cell adhesion in health and disease.

Introduction

Many physiological processes rely on cell adhesion to the surrounding extracellular environment, thereby controlling fundamental cellular behavior, such as cell proliferation, differentiation, survival, and motility. Cell adhesion to the extracellular matrix is fundamental for embryogenesis and for the development and function of a large number of organs, such as the vascular and immune systems. Moreover, proteins that control cell adhesion are often mutated in diseases that are caused by disturbed cell migration, such as metastatic cancer.

Given their important roles in health and disease, cell adhesions have been extensively studied. More than 40 years ago, Abercrombie et al. described in great detail the movement of fibroblasts as they migrated on extracellular-matrix-coated glass cover slips [1-4]. Since then, the main model system to investigate the fundamental mechanisms of cell migration and adhesion has been two-dimensional cultures of fibroblasts on glass [5].

Under these conditions, cell adhesion to the extracellular matrix is mediated through micrometer scale structures that are enriched in adhesion proteins, called focal adhesions (FAs). These FAs physically link the cell to the extracellular environment, propagate mechanical cues, and elicit biochemical signaling events in the cell that control cell functions. More than 150 components, and 380 potential binding interactions can act within FAs [6]. Thus, FAs are considered to be complex multiprotein assemblies that are involved in the control of cell behavior.

Although the biochemical signaling events that involve FAs have been extensively studied, the nanoscale organization of proteins within focal adhesions have for long remained unclear. A number of recent studies have used super-resolution PALM or dSTORM microscopy techniques to determine the spatial localization of proteins within FAs at the nanometer scale [7]. These two techniques are based on the principle that the ectopically expressed, fluorescently tagged molecules are photoactivated and the detected signal computationally processed to render an image. Using this approach, several studies indicate that at the nanoscale level, single fluorescently tagged proteins are localized in a punctuate pattern [8-12]. However, the spatial organization and the co-localization of different endogenous proteins within FAs at the nanometer scale has not been fully identified.

Co-localization algorithms are extensively used in biological studies in order to determine the extent of interaction between different molecular species. However, these algorithms can be highly influenced by the resolution of the system and the density of the labeled samples. Therefore, in a recent study, we evaluated and compared several co-localization algorithms by applying them to both simulated data and specific control samples in order to determine the algorithms best suited for high resolution STED measurements [13]. Image cross correlation spectroscopy (ICCS) is most suitable for analyzing signals of different quantities and provide the best results, in particular when combined with an automated threshold algorithm [13, 14]. Correlation-based methods, such as Pearson correlation coefficient and ICCS, not only depend on the green and red intensity in the individual pixels, but also on how the distributions of these green and red intensities are correlated with each other over the whole image. Non-correlation-based methods analyze only the pixel-wise coincidence of the intensity fluctuations, which to a larger extent is influenced by accidental fluctuations. However, scrutinizing similarities of green and red intensity fluctuations across the entire area by calculating a correlation function can greatly improve the reliability in quantifying the degree of co-localization. Hence, although an increase of the density of red and green labels in the image leads to increased red, green as well as overlapping (yellow) intensities, the calculated correlation-based co-localization value will still be very little affected. Similarly, the spatial resolution will not greatly influence the co-localization data obtained. Further, random noise or even random unspecific binding of the labeled antibodies or Ig aggregates will have little effect on the correlations since the positions of the non-specifically bound antibodies are random. Therefore, they will not result in correlations within or between the different intensity signals. However, although the Pearson algorithm is robust against density or low resolution it is a one-value method, and the results will therefore be difficult to interpret if the molecular quantities are very different in two different channels. In contrast, the ICCS analysis determines the spatial correlation between pixels in different channels of an image, and is therefore advantageous when molecular quantities in two channels differ significantly. In the recent study [13], we evaluated a number of co-localization estimation techniques, combined with automatic threshold setting algorithms, based on a previously published concept to take uncorrelated noise into account [14]. Taken together with our study where we tested and ensured that our method is not affected by signal densities at STED resolution [13], this suggests that ICCS is a reliable quantification method of co-localization for this study.

To determine the nanoscale organization within FAs, we imaged the localization of key FA marker proteins using two- and three- color super-resolution stimulated emission depletion (STED) microscopy,

which can provide resolution down to tens of nanometers. This allowed us to use ICCS to computationally analyze the distribution and co-localization of endogenous focal adhesion markers. Our observations indicate that FAs are composed of nanoscale units of adhesion protein particles in which actomyosin-dependent forces provide non-random control of the localization of different proteins.

Results

Three-color STED microscopy of focal adhesions

When attached to extracellular-matrix-coated glass, fibroblasts develop distinct and wide actomyosin stress fibers that terminate in pronounced FAs. To clarify the nanoscale organization of different FA components in cells, we analyzed FAs at the leading edge of human fibroblasts 48 h after their seeding onto glass. We thus monitored the spatial distribution of four proteins that are known to localize to, and control the functions of, FAs: vinculin, paxillin, β3 integrin, and talin [15]. Much of the biochemical signaling events that occur at the cell surface in fibroblasts take place at FAs, and as a result, kinase activities and tyrosine phosphorylated proteins are enriched in these areas. Therefore, we also studied the distribution of phosphorylated tyrosine residues as a marker for FAs.

To allow clear identification of FAs, we analyzed their spatial localization along filamentous (F-) actin at 40-nm resolution by three-color STED microscopy, utilizing a recently demonstrated imaging approach that exploits differences in photo-stability between different fluorophores [16]. As expected, we observed enrichment of FA proteins at the ends of stress fibers, which identified these areas as FAs (Fig. 1 and Fig. 2).

Intracellular forces regulate co-localization of focal adhesion components

Vinculin is a canonical adhesion-associated protein that is a central component in force transmission in FAs [17, 18]. To determine whether the FA markers co-localize to similar degrees inside compared to between FAs, we analyzed the spatial correlations of vinculin with the other FA proteins studied, using STED microscopy followed by ICCS analysis directly on the STED images. The dynamic range of detectable co-localization using STED microscopy was determined by the use of positive and negative controls. As a positive control for co-localization, we stained vinculin with a primary antibody against vinculin followed

by two different secondary antibodies that were conjugated with separate fluorophores. In this way, we got an estimate of the maximal amount of co-localization detected by this system. As the negative control for co-localization, we co-stained for vinculin and the intermediate filament protein vimentin, which is known to localize to the vicinity of, but not inside, FAs [19-21]. We compared the co-localization of these signals both inside and outside of the areas defined as FAs, based on the density of vinculin and markers in the merged image (Fig. 3). For each sample, we acquired 11 to 15 images, each of which contained two to five adhesion zones, as shown in figure 4A. These images show vinculin as red fluorescence and the other FA markers as green fluorescence (Fig. 4A). They were then analyzed computationally by ICCS method. In the FAs, the positive control yielded co-localization values of ~60% (Fig. 4B). It is important to note that the positive control did not yield 100% co-localization, but a maximum of 60%. This discrepancy between the theoretical and experimentally observed maximal co-localization value is most likely due to that the optical resolution of our microscope (~40 nm) approaches the sizes of primary and secondary antibodies (~10 nm each) and steric hindrance between the antibodies can also increase the inter-fluorophore distances [13]. In these FAs, vinculin showed a similar level of co-localization to paxillin (~30%) and β3 integrin (~30%), followed by talin (~25%) and phosphotyrosine (~20%) (Fig. 4B). Therefore, we concluded that a significant fraction of the FA proteins were co-localized in these FAs. In the areas outside the FAs, the co-localization of vinculin with these markers was significantly reduced, with the p-values for co-localization inside and outside FAs given in Table 1, A, left panel. In the areas outside the FAs, the highest level of vinculin co-localization was to paxillin (~15%), followed by β3 integrin (~10%), talin (~7%), and phosphotyrosine (<5%). The talin and phosphotyrosine co-localization was in the same range as that of the negative control. Thus, we observed different levels of co-localization between vinculin and the different markers, with the corresponding p-values shown in Table 1.

To normalize the levels of co-localization to the maximal and minimal obtainable values, we set the co-localization ratio of the positive control to 100%, and that of the negative control to 0%. The vinculin co-localization coefficients to the other adhesion markers after normalization according to these controls are shown in figure 4C. After normalization, the FAs showed co-localization of vinculin with paxillin and β3 integrin of ~50% to 55%, compared to ~35% with talin and phosphotyrosine (Fig. 4C). We further observed that outside the FAs, the level of vinculin co-localization with paxillin was ~20%, with β3 integrin ~10%, and with talin ~7%. Of note, vinculin showed no co-localization with phosphotyrosine (Fig. 4C). The ICCS method that was used to quantify these co-localizations is not sensitive to the density of the labels, noise

levels, or intensity variations [13], as noise and random intensity variations are not correlated and thus do not contribute to the coefficients determined using this method. Therefore, the higher degree of co-localization inside FAs, as compared to outside FAs, indicates that at the molecular level, these markers are positioned to a greater degree at the same nanoscale site inside FAs, compared to outside FAs.

Different proteins can have different binding partners and be expressed in different absolute quantities, while the amount of a bound complex is of a finite level. This means that the binding fractions of protein A with protein B might not necessarily be equal to those of protein B with protein A. Therefore, it is important to consider both the red co-localization with the green marker, and the green co-localization with the red marker. We also analyzed the extents to which the markers showed in green in the images (as paxillin, β3 integrin, talin, and phosphotyrosine) co-localized with vinculin, including both the positive and negative controls. We observed that these components showed similar co-localization with vinculin in FAs, which were all at >35%, with no statistically significant differences between them. The co-localization of paxillin, talin, and phosphotyrosine with vinculin was significantly lower outside FAs as compared to inside FAs (Table 1). We observed ~20% co-localization with vinculin by these markers, and lower co-localization of β3 integrin with vinculin, at ~10% (Fig. 5A). After normalization to the positive and negative controls, we observed that within FAs, the co-localization of paxillin, β3 integrin, talin, and phosphotyrosine with vinculin was 45% to 70% (Fig. 5B). Outside the FAs, the normalized co-localization of paxillin, talin, and phosphotyrosine with vinculin was slightly less than 40%, and to that of β3 integrin at ~15% (Fig. 5B). The p-values corresponding to these differences in co-localization between the protein pairs are shown in Table 2.

After normalization against the positive and negative controls, the sum of the fractions of vinculin engaged in binding with the three adhesion proteins paxillin, β3 i ntegrin, and talin exceeded 100% (Fig. 4C, 5B ~140%). We further observed that, while co-localization of phosphotyrosine with vinculin was high (Fig. 5B), co-localization of vinculin with phosphotyrosine was low (Fig. 4C). This suggests that while vinculin is present where tyrosine kinase activities are elicited inside FAs, the largest fraction of vinculin inside FAs is localized in areas with no tyrosine kinase activity. This observation supports the concept that vinculin is important for signaling events within FAs.

To determine whether actomyosin contractile forces can regulate the nanoscale organization of adhesions, these cells were treated with the specific myosin II inhibitor blebbistatin, followed by super-

resolution imaging and computational image-analysis. In comparison to the non-treated cells, blebbistatin-treated cells showed a marked reorganization of the spatial distribution of the FA markers (Fig. 6A). While both confocal and STED microscopy showed a redistribution of the markers, only STED microscopy allowed a detailed nanoscale analysis of the spatial redistribution, which often showed an increased localization of the markers at the cell periphery upon blebbistatin-treatment (Fig. 7). Upon blebbistatin-treatment, the markers were slightly enriched at the very edge of the cells (Fig. 6A). This was despite the fact that blebbistatin greatly reduces the thickness at the cell periphery, and the markers therefore are expected to be more widely distributed at the periphery, than at a more central localization of blebbistatin-treated cells, or in non-treated cells. This localization of the marker was similar to the localization in fibroblasts overexpressing another agent linked to reduced RhoA-acto-myosin-mediated contractile forces; the activity of the Rho GTPase Rac1 (Fig. 6A, lower panel) [22]. Using STED microscopy followed by ICCS to compare the colocalization of vinculin to markers, and marker to vinculin, between blebbistatin-treated and non-treated cells, we observed a general decrease in co-localization between the markers in blebbistatin-treated cells (Fig. 4B, Fig. 5A *versus* Fig. 6 B, C, Table 3). This observation that the co-localization between vinculin and focal adhesion markers depends on an actomyosin-driven force is in line with previous observations [17, 23-25].

Intracellular forces have non-random control on the distances between the focal adhesion components

A separate approach to quantify the nanoscale organization of FAs is to measure the distances between FA markers using nearest neighbor analysis. This method is commonly applied to high resolution studies where single targets become visible and therefore the distance between individual targets can be calculated. In contrast to the co-localization analysis, nearest neighbor analysis is more dependent on the density of the labeled targets but provides useful information regarding their nanoscale organization. We used nearest neighbor analysis to determine the extent to which these marker proteins localize within distances that match the size of the adhesion-related particles. The reported size of these particles is approximately 25 nm in diameter [26]. Taken together with the sizes of the primary and secondary antibodies for the immuno-fluorescence labeling that are approximately 10 nm each, and the 40 nm resolution of the microscope, we expect that the signals from proteins which are likely to reside within the same particle to be detected within a distance of 60 nm from each other. We compared the probability that vinculin and the markers were localized within 60 nm in non-treated and blebbistatin-treated cells. Here, in blebbistatin-treated cells, we

observed a significant decrease in the fraction of all of the markers localized proximal to each other in the FA areas (Fig. 8A). In contrast, when comparing the areas outside FAs, blebbistatin treatment resulted in increased probability of vinculin, paxillin, talin, and phosphotyrosine, but not of β3 integrin, to reside within 60 nm of vinculin (Fig. 8A). The corresponding p-values are shown in Table 4. This increase can be attributed to the redistribution of these molecules after blebbistatin-induced spatial redistribution of FA markers.

We further analyzed how blebbistatin influenced the distances between the different FA markers with other molecules of the same marker (i.e., marker-to-self distances). We observed that as compared to the marker-to-self distances in areas within FAs in non-treated cells, blebbistatin-treated cells showed increased fractions for paxillin and talin, but not for integrin and phosphotyrosine. When compared to the marker-to-self distances in areas outside FAs in non-treated cells, blebbistatin-treated cells showed increased probabilities for integrin, talin, and phosphotyrosine, but not for paxillin (Fig. 8B). The corresponding p-values are shown in Table 4.

When comparing the distances between markers in the FAs of non-treated cells to blebbistatin-treated cells, we observed that blebbistatin decreased the 60-nm proximal fractions of the markers to the other types of markers, while it increased the marker-to-self fractions (Fig. 8). Thus, blebbistatin decreased the distances between proteins of the same type, i.e. the homo-molecular distances displayed by the species in their short-range organization. A random redistribution of FA markers in areas outside FAs upon blebbistatin treatment would not lead to decreased homo-molecular distances, to levels that are comparable to, or smaller than, inside FAs. This was further demonstrated by computational simulations of images with randomized distribution (Fig. 9). We observed that the markers were sometimes positioned at a more peripheral location of the cell (Fig. 6A). We therefore speculate that loss of intracellular forces results in a redistribution of the markers that is not random. We further observed a bipolar behavior of the distance change between the markers upon blebbistatin treatment (see nearest neighbor data in Fig. 10A). This bipolar behavior and the observation that blebbistatin increased the hetero-molecular distances while it decreased the homo-molecule distances would indicate that when blebbistatin releases the strain over the adhesions, the different types of molecules that in untreated cells are bridged by mechanical forces move apart, whereas the same molecules move closer to each other.

Discussion

To our knowledge, our STED three-color super-resolution images are the first to show the nanoscale localization of three endogenous proteins in a focal adhesion. Our data support the concept that adhesion proteins in FAs are organized into nanoscale protein particles. These data also indicate that actomyosin-generated forces exert a non-random control of the localization of proteins to these nanoscale protein particles.

Our study demonstrates that at ~30% of the sites where vinculin was localized, three (or more) different adhesion proteins were present. This indicates that there are protein particles that contain at least these three analyzed proteins (and possibly more) inside the FAs. This observation is in agreement with earlier findings by the Medalia group, who used electron microscopy to show that adhesion proteins in FAs are organized in 25-nm units, which they named focal adhesion-related particles; FARPs [26]. Our observations support the concept that adhesion proteins in FAs are organized into distinct nanoscale particles, such as FARPs, and this concept is supported by other studies that have demonstrated subdomains and punctuate distributions of adhesion proteins within FAs [9, 10, 27-29].

In a recent publication, Hu et al. used structured illumination microscopy to report that FAs appear to be composed of smaller subunits that are organized as elongated, typically 300-nm wide, subunits along the actin filaments [30]. We do not observe such subunits to be a general pattern, and the difference in observation could be attributed to our different experimental conditions, such as different extracellular ligands or time allowed to attach and spread. Notably, while their analysis was performed 3 hours post seeding, our cells had been allowed to adhere and spread for 48 hours prior to analysis. We therefore expect that our extended incubation time result in adhesions that are more similar to fibrillar adhesions than the adhesions studied by Hu et al.

We showed here that the nanoscale co-localization of the FA markers was very different in FAs as compared to the areas outside FAs, with greater nanoscale co-localization in FAs. β3-Integrin binding to the extracellular matrix is considered to be an initial event that is required for accumulation of additional FA components. In agreement with this, Kanchanawong et al. observed that when analyzed at the nanoscale level, the integrins are localized closer to the glass surface than the other FA components [28]. In the

present study, the higher degree of co-localization between vinculin and the other proteins in FAs, compared to the non-FA areas, was most pronounced for β3-integrin. This might indicate an absolute requirement for β3-integrin to form the functional sites of these adhesive multi-protein complexes inside FAs. This is consistent with the observation of Rossier et al., who also worked at the nanoscale level to show that β3-integrin is stationary inside FAs [31]. The observation that the degree of co-localization between the analyzed FA components was significantly lower outside FAs indicates that these nanoscale sites of cell adhesion are predominantly inside FAs. This is consistent with earlier observations that integrin inhibitors can be bound to integrins outside FAs, and displaced by integrin activators enriched in FAs [32]. Extracellular matrix composition, dimensionality, and mechanical cues control cell adhesion, and the adhesive structures can be significantly smaller than FAs [33]. Recent findings have shown that the matrix architecture and the nanoscale distances between ligands control their cellular responses [34], and that nanoscale focal adhesion particles are more densely packed in the FAs of fibroblasts lacking integrin-linked kinase [35].

Together with the present data and previous reports showing nanoscale point-like distributions of adhesion markers, we hypothesize that the local concentrations and spatial distributions of the separate nanoscale units of adhesive protein particles constitute the basis of cell adhesion *in vivo*, and anticipate that nanoscale structural and co-localization analyses of FAs will become commonly used in studies of FAs function and structure.

We observed that at the nanometer scale, blebbistatin-treatment resulted in a slightly more peripheral localization of focal adhesion markers, reduced co-localization and increased distances between markers of different types. As described in figure 11, we suggest that intracellular forces to a higher extent promote the co-localization of different focal adhesion markers to each other, than the co-localization between markers of the same type. To our knowledge, these are the first results that indicate this possibility. We propose that mechanical forces result in that different molecules interact, and that loss of force upon blebbistatin-treatment therefore causes molecules of the same type move closer to each other during a dissassembly of the FA. We observed that blebbistatin-treatment induced a relocalization of the adhesion markers that was similar to observed in constitively active Rac1 expressing cells. However, we would like to stress that although both these agents control adhesions, it is most likely by different mechanism and at different time scales. We do not exclude the possibility that interactions with the ECM, force-dependent changes of the

organization of the actin cytoskeleton, forces that remain after blebbistatin-treatment, or possible blebbistatin-induced effects that are independent of acto-myosin contractile forces, can contribute to the blebbistatin-induced re-distribution that we observe.

Taken together, our data are consistent with the hypothesis that FA components are structurally organized into nanoscale sites of protein assemblies or particles within, and not outside of, FAs. The data highlight the possibility that intracellular forces exert a non-random control of the spatial organization of proteins in these nanoscale multiprotein particles. This detailed knowledge of the organization of cell-matrix adhesion at the nanometer scale increases our understanding of the physiological and pathophysiological processes that depend upon cell adhesion, such as embryogenesis and cancer progression.

Materials and Methods

Cell culture and plating and transfection

Human primary skin fibroblasts at passage 55, ATCC® CRL-2522™, donated as described at the nonprofit biological resource center ATCC; http://www.lgcstandards-atcc.org/en.aspx, and in [36-39] were cultured in Dulbecco's modified Eagle's medium and 10% fetal bovine serum (both from HyClone, Thermo Fisher Scientific, Waltham, USA) in a cell incubator, under 5% CO_2 at 37 °C. These cells were plated onto glass coverslips in a cell culture dish containing culture medium, and left to spread for 48 h prior to treatment and analysis. Expression and analysis of constitutively active GFP-conjugated Rac1L61 was performed in NIH3T3 fibroblasts, as described previously [40]. Cells were treated for one hour with 10μg/ml blebbistatin (Sigma-Aldrich, St Louis, USA) in cell culture media in the cell incubator, prior to analysis.

Immunofluorescence staining

The cells were fixed in 3.7% paraformaldehyde for 15 min at 37 °C, and then permeabilized with 0.2% Triton X100 for 5 min at room temperature. The cover-slips with the cells were then washed in phosphate-buffered saline (PBS) for 10 min, and blocked in 1% bovine serum albumin in PBS for 1 h at room temperature. The anti-vimentin antibody for the negative control (V9; Sigma-Aldrich) was diluted 1:175 in 0.1% bovine serum albumin in PBS. Similarly, using 0.1% bovine serum albumin in PBS, the anti-

phosphotyrosine antibody (PY99; Santa Cruz Biotechnology, Santa Cruz, USA) was diluted 1:100, the anti-paxillin antibody (Clone 349; BD Transduction Laboratories) 1:500, the anti-vinculin antibody (V4139; Sigma-Aldrich, St Louis, USA) 1:100, the anti-β3-integrin antibody (CD61; GTI Diagnostics) 1:100, and the anti-talin antibody (Clone 8d4; Sigma-Aldrich) 1:200. Monoclonal and polyclonal antibodies conjugated with Atto-590 and Atto-647N were used (Atto-tec GmbH, Siegen, Germany, labeled by Anna Perols, Biotech, KTH, Stockholm, Sweden) at 4 μg/ml, to stain the primary vinculin antibodies for the positive control. For the negative control, the same polyclonal secondary antibody against vinculin labeled with Atto-647N was used, together with Atto-590–coupled secondary antibodies against vimentin. After the staining, the cells were washed by gentle shaking in PBS for 30 min at room temperature. The cover-slips were then dipped in double-distilled H_2O, and mounted on a microscope slide using a mounting solution of 0.3 mg/ml glycerol and 0.12 mg/ml Mowiol in 60 mM Tris at pH 8.5.

STED microscopy

The STED microscope had two separate excitation beams of 570 ±5 nm and 647 ±5 nm, and two STED beams of 710 ±10 nm and 750 ±10 nm. Fluorescence was collected using two separate spectral channels of 615 ±15 nm and 675 ±15 nm. The STED beams passed through separate vortex phase plates (VPP-1; RPC Photonics, Rochester, NY, USA) to provide a donut transverse mode, such that excited molecules outside of the central minimum of the STED beam were stimulated back to the ground state, to leave only the very central molecules to fluoresce. The excitation and STED beams came from the same pulsed supercontinuum Fianium laser (SC-450-PP-HE; Fianium Ltd., Southampton, UK). The laser was set to 1 MHz frequency and the pulse duration was ~100 ps. To reduce spectral crosstalk, a time delay of 40 ns was set between the excitation and STED beams of the two different color channels. The laser power for imaging was set to 200 nW to 500 nW for the excitation wavelengths, and to 0.8 mW to 1.4 mW for the STED wavelengths. Although this set-up had only two color channels, the separation of up to four target molecules was possible using the differences in the photo-stabilities of the fluorescent dyes, despite their similar spectra ranges, as shown previously [16]. The bleaching power for ATTO-647N coupled to phalloidin was set to 1 mW at 710 ±10 nm, which was more than two orders of magnitude greater than the excitation power used for imaging. The image size was set to 10 ×10 μm^2, with a pixel size (also known as the scanning step size) of 10 nm for the STED images and 50 nm for the confocal images, and a pixel dwell time of 1 ms. The intensity levels of the channels in all of the merged color images were adjusted using the automatic settings of Adobe Photoshop. The resolution for each of the three colors in our system is 40nm.

Cell image processing

The immunofluorescence images were acquired using the Imspector software (Department of NanoBiophotonics, Max Planck Institute for Biophysical Chemistry, Göttingen, Germany), and exported as .dat files. This preserved each value of each pixel as the number of the originally detected photons in that pixel. The exported file was then imported and processed in MATLAB. Immuno-fluorescence images were first converted to binary images using the MATLAB 'graythresh' function. Then the cell boundaries and cell-matrix adhesion zones were identified using the MATLAB 'imdilate' function, with different sizes of disk-shaped structural elements, such that sparsely distributed fluorescence was separated from areas where the fluorescence intensities were more densely localized (Fig. 3). The choice of the disk-shape structural element sizes for the image dilation processes was based on empirical trials. As these areas could be identified separately, this allowed the extent of co-localization to be calculated specifically for cell-matrix adhesion and non-adhesion zones, as well as to discard irrelevant non-specific fluorescence staining at the glass surface outside the cell boundary. We created differentially identified areas as mask functions, which with simple multiplication were combined with co-localization calculations and nearest neighbor analysis methods.

Co-localization calculations

Automatic threshold search: The automatic threshold search algorithm used a percentile function to set the threshold iteratively, until the pixels below the intensity threshold returned by the percentile threshold reached a Pearson correlation of zero, to indicate no correlation [13, 14]. Once the percentile threshold was defined, the intensities below the threshold were discarded as noise, and the remaining pixels were kept for further co-localization analysis.

Co-localization algorithms

The Pearson correlation coefficient has its mathematical definition as in Equation (1):

$$P = \frac{\sum (R_i - \bar{R}) \times (\mathrm{G}_i - \bar{\mathrm{G}})}{\sqrt{\sum (R_i - \bar{R})^2 \times (\mathrm{G}_i - \bar{\mathrm{G}})^2}} \quad (1),$$

where R_i and G_i are the intensities at pixel i in the red and green channels, respectively, and the horizontal bar denotes a mean operator for the corresponding channel.

The co-localization ratios defined by the ICCS approach [41] in the red and green channels were calculated as in Equation (2):

$$ICCS_{red} = \frac{r_{rg}(0,0)}{r_{gg}(0,0)}, ICCS_{green} = \frac{r_{rg}(0,0)}{r_{rr}(0,0)} \quad (2),$$

where $r_{rg}(0,0)$ is the spatial cross-correlation amplitude for the red and green channel images at zero pixel lags, and $r_{rr}(0,0)$ and $r_{gg}(0,0)$ are the spatial auto-correlation amplitudes for the red and green channels, respectively. The spatial correlation function was defined as in Equation (3):

$$r_{kl}(\varepsilon,\eta) = \frac{\langle \delta I_k(x,y) \times \delta I_l(x+\varepsilon, y+\eta) \rangle}{\langle I_k \rangle \times \langle I_l \rangle} \quad (3),$$

where the subscripts k and l are detection channels k and l, which can be either the same or different in terms of the autocorrelation and the cross-correlation calculations, respectively.

The spatial correlation function was fitted using a two-dimensional Gaussian function, as in Equation (4):

$$r_{kl}(\varepsilon,\eta) = r_{kl}(0,0)\exp\left(\frac{-(\varepsilon+u)^2}{w_x^2} + \frac{-(\eta+v)^2}{w_y^2}\right) + r_\infty \quad (4),$$

where w_x^2 and w_y^2 are the laser beam radii for the x and y direction, respectively, and r_∞ is the off-set. The ICCS coefficients shared the same numerator, which was a function of the fluorescence labeling and physical binding of interacting molecules, while the spatial autocorrelation functions in the denominators were related to the point spread functions of the imaged points. This method is similar to more original approach called scanning correlation spectroscopy [42] and later on a method called raster image correlation spectroscopy (RICS) [43]. As a note, RICS has been both used combined with STED [44] and complementarily to STED imaging [45]. In this paper, the ICCS analysis is directly performed on STED images.

448

449 **Nearest neighbor analysis**

450 The nearest neighbor analysis was carried out by first identifying the peaks in the deconvoluted STED
451 fluorescence images using a conventional supervised approach, and then running a home-written script to
452 perform nearest neighbor distance calculations on the identified peaks, as in [46]. All calculations done on
453 experimental images were carried out in MATLAB.

454

455 **Simulation of fluorescence images**

456 The simulation of fluorescence images with different degrees of randomized distribution inside cell
457 adhesions and in whole cells as well as the subsequent calculation of nearest neighbor histograms were
458 performed with GNU Octave 4.0.3 together with extra associated Octave-Forge packages: geometry,
459 communications and image. All simulated images have a size of 10 X 10 μm^2 with 1000 X 1000 pixels and
460 equal particle numbers of 2500 in each cell. For simulating confocal and STED images, dot images were
461 first generated and were then convoluted with Gaussian-type point spread functions of different widths
462 corresponding to 40 and 250 nm resolutions. Neither noise nor optical aberrations were added to the images.
463 For partially randomized protein distributions within focal adhesions, half of the proteins were completely
464 spatially randomized, while the other half of the proteins were organized into clusters with radii of 50 nm,
465 each cluster on average containing 4 member proteins. The parameters were chosen arbitrarily as the
466 intention for the simulation was not to reproduce the experimental data but to show how the spatial
467 distribution organization of different proteins can affect the analytical results. The histograms were
468 accumulated from nearest neighbor analysis of 5 sets of simulated dot images.

469

470 ## Statistical analysis

471 The cells were imaged from three separately prepared samples at different dates for all of the experimental
472 samples. In all, 11 to 15 images were analyzed for each case. All of the error bars in the figures are given as
473 standard deviation (SD), as determined from the whole sample set, of n = 11 to 15. Two-tailed *t*-tests with
474 unequal variances were used to determine the significant differences, as the p-values, of the co-localization
475 ratios within FAs and outside FAs.

476

477

Acknowledgements

The authors would like to thank Dr William C. Hahn (Harvard Medical School, Boston, MA, USA) for the BJ cells, Syskonen Svenssons foundation and Ollie and Elof Ericssons Foundation for financial support to AG. PA was supported by the Swedish Cancer Society. Knut and Alice Wallenberg Foundation (KAW 2011.0218) is acknowledged for the financial support of the STED instrumentation (to JW). This article was also supported by Fundação para a Ciência e a Tecnologia (FCT) with funds from the Portuguese Government (PEst-OE/QUI/UI0674/2013) and by the ARDITI- Agência Regional para o Desenvolvimento da Investigaçaõ Tecnologia e Inovação through the project M1420-01-0145-FEDER-000005 - Centro de Química da Madeira - CQM+ (Madeira 14-20).

Author contribution

L. Xu, D. Rönnlund, J. Widengren, P. Aspenström and A. K. B Gad designed research; L. J. Braun, L. Xu, D. Rönnlund, A. K. B. Gad performed research; L. Xu contributed new analytic tools; L. Xu, D. Rönnlund, J. Widengren, P. Aspenström and A. K. B. Gad analyzed data; L. Xu, J. Widengren and A. K. B. Gad wrote the paper.

References

1.Abercrombie M, Heaysman JE, Pegrum SM. The locomotion of fibroblasts in culture. I. Movements of the leading edge. Experimental cell research. 1970;59(3):393-8. Epub 1970/03/01. PubMed PMID: 4907703.

2. Kardash, E., Reichman-Fried, M., Maitre, J. L., Boldajipour, B., Papusheva, E., Messerschmidt, E. M., Heisenberg, C. P. & Raz, E. (2010) A role for Rho GTPases and cell-cell adhesion in single-cell motility in vivo, *Nature Cell Biology.* **12**, 47-53; sup pp 1-11.

3. Abercrombie, M., Heaysman, J. E. & Pegrum, S. M. (1970) The locomotion of fibroblasts in culture. I. Movements of the leading edge, *Experimental cell research.* **59**, 393-8.

4. Abercrombie, M., Heaysman, J. E. & Pegrum, S. M. (1970) The locomotion of fibroblasts in culture. II. "Ruffling", *Experimental cell research.* **60**, 437-44.

5. Sixt, M. (2012) Cell migration: fibroblasts find a new way to get ahead, *The Journal of cell biology.* **197**, 347-9.
6. Geiger, T. & Zaidel-Bar, R. (2012) Opening the floodgates: proteomics and the integrin adhesome, *Current opinion in cell biology.* **24**, 562-8.
7. Schwartz, M. A. (2011) Super-resolution microscopy: a new dimension in focal adhesions, *Curr Biol.* **21**, R115-6.
8. van Hoorn, H., Harkes, R., Spiesz, E. M., Storm, C., van Noort, D., Ladoux, B. & Schmidt, T. (2014) The nanoscale architecture of force-bearing focal adhesions, *Nano Lett.* **14**, 4257-62.
9. Shroff, H., Galbraith, C. G., Galbraith, J. A., White, H., Gillette, J., Olenych, S., Davidson, M. W. & Betzig, E. (2007) Dual-color superresolution imaging of genetically expressed probes within individual adhesion complexes, *Proceedings of the National Academy of Sciences of the United States of America.* **104**, 20308-20313.
10. Shroff, H., Galbraith, C. G., Galbraith, J. A. & Betzig, E. (2008) Live-cell photoactivated localization microscopy of nanoscale adhesion dynamics, *Nature Methods.* **5**, 417-423.
11. Chien, F. C., Kuo, C. W., Yang, Z. H., Chueh, D. Y. & Chen, P. (2011) Exploring the formation of focal adhesions on patterned surfaces using super-resolution imaging, *Small.* **7**, 2906-13.
12. Case, L. B., Baird, M. A., Shtengel, G., Campbell, S. L., Hess, H. F., Davidson, M. W. & Waterman, C. M. (2015) Molecular mechanism of vinculin activation and nanoscale spatial organization in focal adhesions, *Nat Cell Biol.* **17**, 880-92.
13. Xu, L., Ronnlund, D., Aspenstrom, P., Braun, L. J., Gad, A. K. B. & Widengren, J. (2016) Resolution, target density and labeling effects in colocalization studies - suppression of false positives by nanoscopy and modified algorithms, *Febs Journal.* **283**, 882-898.
14. Costes, S. V., Daelemans, D., Cho, E. H., Dobbin, Z., Pavlakis, G. & Lockett, S. (2004) Automatic and quantitative measurement of protein-protein colocalization in live cells, *Biophysical Journal.* **86**, 3993-4003.
15. Wehrle-Haller, B. (2012) Structure and function of focal adhesions, *Current opinion in cell biology.* **24**, 116-24.
16. Ronnlund, D., Xu, L., Perols, A., Gad, A. K., Eriksson Karlstrom, A., Auer, G. & Widengren, J. (2014) Multicolor fluorescence nanoscopy by photobleaching: concept, verification, and its application to resolve selective storage of proteins in platelets, *ACS Nano.* **8**, 4358-65.
17. Grashoff, C., Hoffman, B. D., Brenner, M. D., Zhou, R. B., Parsons, M., Yang, M. T., McLean, M. A., Sligar, S. G., Chen, C. S., Ha, T. & Schwartz, M. A. (2010) Measuring mechanical tension across vinculin reveals regulation of focal adhesion dynamics, *Nature.* **466**, 263-U143.
18. Rubashkin, M. G., Cassereau, L., Bainer, R., DuFort, C. C., Yui, Y., Ou, G. Q., Paszek, M. J., Davidson, M. W., Chen, Y. Y. & Weaver, V. M. (2014) Force Engages Vinculin and Promotes Tumor Progression by Enhancing PI3K Activation of Phosphatidylinositol (3,4,5)-Triphosphate, *Cancer Research.* **74**, 4597-4611.
19. Zamir, E. & Geiger, B. (2001) Components of cell-matrix adhesions, *Journal of Cell Science.* **114**, 3577-3579.
20. Ronnlund, D., Gad, A. K., Blom, H., Aspenstrom, P. & Widengren, J. (2013) Spatial organization of proteins in metastasizing cells, *Cytometry A.* **83**, 855-65.
21. Leube, R. E., Moch, M. & Windoffer, R. (2015) Intermediate filaments and the regulation of focal adhesion, *Current Opinion in Cell Biology.* **32**, 13-20.
22. Kuo, J. C., Han, X., Hsiao, C. T., Yates, J. R., 3rd & Waterman, C. M. (2011) Analysis of the myosin-II-responsive focal adhesion proteome reveals a role for beta-Pix in negative regulation of focal adhesion maturation, *Nat Cell Biol.* **13**, 383-93.
23. Cohen, D. M., Kutscher, B., Chen, H., Murphy, D. B. & Craig, S. W. (2006) A conformational switch in vinculin drives formation and dynamics of a talin-vinculin complex at focal adhesions, *Journal of Biological Chemistry.* **281**, 16006-16015.
24. Golji, J., Wendorff, T. & Mofrad, M. R. K. (2012) Phosphorylation Primes Vinculin for Activation, *Biophysical Journal.* **102**, 2022-2030.
25. Humphries, J. D., Wang, P., Streuli, C., Geiger, B., Humphries, M. J. & Ballestrem, C. (2007) Vinculin controls focal adhesion formation by direct interactions with talin and actin, *Journal of Cell Biology.* **179**, 1043-1057.

555 26. Patla, I., Volberg, T., Elad, N., Hirschfeld-Warneken, V., Grashoff, C., Fassler, R., Spatz, J. P., Geiger, B. & Medalia,
556 O. (2010) Dissecting the molecular architecture of integrin adhesion sites by cryo-electron tomography, *Nature Cell*
557 *Biology.* **12**, 909-15.
558 27. van Hoorn, H., Harkes, R., Spiesz, E. M., Storm, C., van Noort, D., Ladoux, B. & Schmidt, T. (2014) The Nanoscale
559 Architecture of Force-Bearing Focal Adhesions, *Nano Letters.* **14**, 4257-4262.
560 28. Kanchanawong, P., Shtengel, G., Pasapera, A. M., Ramko, E. B., Davidson, M. W., Hess, H. F. & Waterman, C. M.
561 (2010) Nanoscale architecture of integrin-based cell adhesions, *Nature.* **468**, 580-4.
562 29. Betzig, E., Patterson, G. H., Sougrat, R., Lindwasser, O. W., Olenych, S., Bonifacino, J. S., Davidson, M. W.,
563 Lippincott-Schwartz, J. & Hess, H. F. (2006) Imaging intracellular fluorescent proteins at nanometer resolution,
564 *Science.* **313**, 1642-1645.
565 30. Hu, S., Tee, Y. H., Kabla, A., Zaidel-Bar, R., Bershadsky, A. & Hersen, P. (2015) Structured illumination microscopy
566 reveals focal adhesions are composed of linear subunits, *Cytoskeleton (Hoboken).* **72**, 235
567 5-45.
568 31. Rossier, O., Octeau, V., Sibarita, J. B., Leduc, C., Tessier, B., Nair, D., Gatterdam, V., Destaing, O., Albiges-Rizo, C.,
569 Tampe, R., Cognet, L., Choquet, D., Lounis, B. & Giannone, G. (2012) Integrins beta1 and beta3 exhibit distinct
570 dynamic nanoscale organizations inside focal adhesions, *Nature Cell Biology.* **14**, 1057-67.
571 32. Moser, M., Legate, K. R., Zent, R. & Fassler, R. (2009) The tail of integrins, talin, and kindlins, *Science.* **324**, 895-9.
572 33. Geiger, B. & Yamada, K. M. (2011) Molecular Architecture and Function of Matrix Adhesions, *Csh Perspect Biol.* **3**.
573 34. Cavalcanti-Adam, E. A., Volberg, T., Micoulet, A., Kessler, H., Geiger, B. & Spatz, J. P. (2007) Cell spreading and
574 focal adhesion dynamics are regulated by spacing of integrin ligands, *Biophysical Journal.* **92**, 2964-2974.
575 35. Elad, N., Volberg, T., Patla, I., Hirschfeld-Warneken, V., Grashoff, C., Spatz, J. P., Fassler, R., Geiger, B. & Medalia,
576 O. (2013) The role of integrin-linked kinase in the molecular architecture of focal adhesions, *J Cell Sci.* **126**, 4099-107.
577 36. Yi, X., Tesmer, V. M., Savre-Train, I., Shay, J. W. & Wright, W. E. (1999) Both transcriptional and
578 posttranscriptional mechanisms regulate human telomerase template RNA levels, *Mol Cell Biol.* **19**, 3989-97.
579 37. Weinrich, S. L., Pruzan, R., Ma, L., Ouellette, M., Tesmer, V. M., Holt, S. E., Bodnar, A. G., Lichtsteiner, S., Kim, N.
580 W., Trager, J. B., Taylor, R. D., Carlos, R., Andrews, W. H., Wright, W. E., Shay, J. W., Harley, C. B. & Morin, G. B. (1997)
581 Reconstitution of human telomerase with the template RNA component hTR and the catalytic protein subunit hTRT,
582 *Nat Genet.* **17**, 498-502.
583 38. Hahn, W. C., Counter, C. M., Lundberg, A. S., Beijersbergen, R. L., Brooks, M. W. & Weinberg, R. A. (1999)
584 Creation of human tumour cells with defined genetic elements, *Nature.* **400**, 464-8.
585 39. Bodnar, A. G., Ouellette, M., Frolkis, M., Holt, S. E., Chiu, C. P., Morin, G. B., Harley, C. B., Shay, J. W., Lichtsteiner,
586 S. & Wright, W. E. (1998) Extension of life-span by introduction of telomerase into normal human cells, *Science.* **279**,
587 349-52.
588 40. Gad, A. K., Ronnlund, D., Spaar, A., Savchenko, A. A., Petranyi, G., Blom, H., Szekely, L., Widengren, J. &
589 Aspenstrom, P. (2012) Rho GTPases link cellular contractile force to the density and distribution of nanoscale
590 adhesions, *FASEB J.* **26**, 2374-82.
591 41. Comeau, J. W., Costantino, S. & Wiseman, P. W. (2006) A guide to accurate fluorescence microscopy
592 colocalization measurements, *Biophysical Journal.* **91**, 4611-22.
593 42. Stpierre, P. R. & Petersen, N. O. (1990) Relative Ligand-Binding to Small or Large Aggregates Measured by
594 Scanning Correlation Spectroscopy, *Biophysical Journal.* **58**, 503-511.
595 43. Petersen, N. O., Hoddelius, P. L., Wiseman, P. W., Seger, O. & Magnusson, K. E. (1993) Quantitation of
596 Membrane-Receptor Distributions by Image Correlation Spectroscopy - Concept and Application, *Biophysical Journal.*
597 **65**, 1135-1146.
598 44. Hedde, P. N., Dorlich, R. M., Blomley, R., Gradl, D., Oppong, E., Cato, A. C. B. & Nienhaus, G. U. (2013) Stimulated
599 emission depletion-based raster image correlation spectroscopy reveals biomolecular dynamics in live cells, *Nat*
600 *Commun.* **4**.
601 45. Dreier, J., Sorensen, J. A. & Brewer, J. R. (2016) Superresolution and Fluorescence Dynamics Evidence Reveal
602 That Intact Liposomes Do Not Cross the Human Skin Barrier, *Plos One.* **11**.

603 46. Blom, H., Ronnlund, D., Scott, L., Spicarova, Z., Rantanen, V., Widengren, J., Aperia, A. & Brismar, H. (2012)
604 Nearest neighbor analysis of dopamine D1 receptors and Na plus -K plus -ATPases in dendritic spines dissected by
605 STED microscopy, *Microsc Res Techniq.* **75**, 220-228.

606

607

Tables

Table 1: Statistical significances for comparisons between the different protein-pair co-localizations inside and outside the FAs, according to ICCS analysis (two-tailed students' *t*-tests, with unequal variance).

Protein pair	Significance of differences between inside and outside FAs	
	Red channel	Green channel
Pax (green)-Vin (red)	3.35E-4	2.33E-4
Int (green)-Vin (red)	2.32E-07	2.81E-12
Tal (green)-Vin (red)	6.63E-4	7.18E-5
pY (green)-Vin (red)	2.34E-07	1.11E-2

Vin, vinculin; Pax, paxillin; Int, β3-integrin; Tal, talin; pY, phosphotyrosine

Table 2: Statistical significances for comparisons of the different protein-pair for their co-localizations inside and outside the FAs, according to ICCS analysis (two-tailed students' *t*-tests, with unequal variance).

Primary protein pair	Secondary protein pair	Significance for comparison between marker pairs			
		Red channel		Green channel	
		Within FAs	Outside of FAs	Within FAs	Outside of FAs
Int (green)-Vin(red)	Pax-Vin	7.66E-2	1.21E-2	5.55E-2	4.74E-3
	Tal-Vin	3.32E-2	0.169	1.70E-2	1.54E-3
	pY-Vin	2.59E-3	9.53E-5	6.33E-2	7.52E-3
Pax (green)-Vin(red)	Tal-Vin	5.31E-3	1.13E-3	0.984	0.755
	pY-Vin	2.81E-3	2.25E-6	0.937	0.444
pY (green)-Vin(red)	Tal-Vin	0.815	2.01E-2	0.914	0.600

Vin, vinculin; Pax, paxillin; Int, β3 integrin; Tal, talin; pY, phosphotyrosine

Table 3: Statistical analysis of co-localization of cell adhesion markers without and with blebbistatin treatment (two-tailed student *t*-tests, with unequal variances). Non-treated cells were analyzed with regard to co-localization inside and outside adhesive zones, and for blebbistatin-treated cells, the whole images were analyzed.

Marker	**Significance for comparison between ±blebbistatin**			
	Vinculin to marker		**Marker to vinculin**	
	Adh	**NonAdh**	**Adh**	**NonAdh**
Paxillin	3.40E-4	0.13	2.10E-7	1.62E-3
β3-Integrin	6.05E-9	3.46E-4	1.15E-13	1.82E-4
Talin	5.47E-05	0.11	5.40E-10	1.33E-4
pY	1.52E-07	0.67	1.17E-6	1.34E-3

pY, phosphotyrosine

Table 4: Statistical analysis of nearest neighbor distance less than 60 nm on cell adhesion markers without and with blebbistatin-treatment (two-tailed student *t*-tests, with unequal variances).

Marker	**Significance for comparison between ±blebbistatin**			
	Vinculin to marker		**Marker to marker**	
	Adh	**NonAdh**	**Adh**	**NonAdh**
Paxillin	8.01E-5	4.05E-2	9.74E-5	0.729
β3-Integrin	1.17E-5	0.269	0.506	6.26E-8
Talin	0.216	9.76E-3	8.88E-3	2.09E-9
pY	1.11E-2	4.29E-2	8.68E-2	1.51E-6

pY, phosphotyrosine

Figure legends

Figure 1. Nanoscale analysis of FA components in fibroblasts using three-color STED microscopy. Representative images of spatial localization of paxillin, vinculin, and F-actin (as indicated). The merged image shows paxillin (green), vinculin (red) and F-actin (blue). Scale bar, 2 μm.

Figure 2. Three color nanoscale analysis of FA components in fibroblasts using STED microscopy. Representative images of the nanoscale spatial localization of β3 integrin, phosphotyrosine (pY), talin and F-actin (as indicated). The merged image shows β3 integrin, phosphotyrosine and talin in green, vinculin (red) and F-actin (blue). Scale bar, 2 μm.

Figure 3. Basis of computational co-localization. In a single cell, the FAs can be isolated from the surrounding area using a home-written MATLAB function. **A**, Original fluorescence STED image of the chosen area of a cell. **B**, Cell boundary identified by the program, to exclude unspecific sparse staining on the glass surface. **C**, FAs, as identified by the density of the fluorescence staining by the program. **D**, Non-adhesion zones inside the cell boundary, obtained from combining (B) and (C). **E,** Cells stained for vinculin and the markers integrin or talin, as indicated. Corresponding images of double stained cells are shown with regard to vinculin (left panel, bold underlined) or markers (right panel, bold underlined), and the areas computationally classified as FA areas (red) and non FA (blue) are shown in the vinculin image (left panel) or marker image (right panel).

Figure 4. Co-localization of vinculin with other FA markers in FAs, compared to areas outside FAs. A, Top panel shows representative images of the spatial localization in FAs of vinculin (red) and paxillin, β3 integrin, talin, or phosphotyrosine (green), as indicated. Scale bar, 2 μm. The corresponding single channel images are shown in the middle and lower panels. FA areas and the cell border are indicated with blue or white lines, respectively. The negative and positive controls for the staining are shown, as indicated. **B,** Quantification of co-localization of vinculin with paxillin (blue), β3 integrin (red), talin (green), and phosphotyrosine (purple), as well as the positive (white) and negative (black) controls in FAs and outside FAs (non FA). *, **, *** denotes $P < 0.05$, 0.01, 0.001, respectively (see also Table 1). **C,** Quantification of co-localization of vinculin with the other adhesion markers after normalization with the positive and negative controls. Data were obtained from 3 to 5 images from 3 independent experiments, for a total of 11 to 15 images for each sample. Each image contained two to five FAs.

Figure 5. Co-localization of paxillin, β3 integrin, talin, and phosphotyrosine with vinculin is higher in FAs. A, Quantification of colocalization of paxillin (blue), β3 integrin (red), talin (green), and phosphotyrosine (purple) with

vinculin in FAs and outside FAs (non FA). *, **, *** denotes P <0.05, 0.01, 0.001, respectively (see also Table 1). **(B)** Quantification of co-localization after normalization to the controls of co-localization. Data were obtained from 3 to 5 images from 3 independent experiments, for a total of 11 to 15 images for each sample. Each image contained two to five FAs.

Figure 6. Blebbistatin-induced effects on colocalization. A, Top panel shows representative images of the spatial localization in blebbistatin-treated cells of vinculin (red) and paxillin, β3 integrin, talin, or phosphotyrosine (green), as indicated. Scale bar, 2 μm. The corresponding single channel images are shown in the middle and lower panels, and the signal at the cell edge (marked by a white line) is indicated by arrows. The small, lower, right panel shows spatial localization of phosphotyrosine (green) and F-actin (red) in NIH3T3 fibroblasts expressing constitutively active Rac1, as indicated. Co-localization of vinculin to cell adhesion markers (**B**), or markers to vinculin (**C**) in cells treated with blebbistatin. The whole images were analyzed for blebbistatin-treated cells.

Figure 7. Representative confocal and STED image data. **A**, Raw confocal image of non blebbistatin-treated cells, showing paxillin (green) and vinculin (red). **B**, The raw STED image of the area shown in A. **C**, Raw confocal image of blebbistatin-treated cells, with paxillin (green) and vinculin (red). **D**, The raw STED image of the area shown in C. Scale bar, 1 μm.

Figure 8. Probabilities of inter-marker distances within the size of an adhesion particle plus the labeling antibodies without and with blebbistatin treatment. Bars show the probabilities inside and outside adhesive zones, as well as for cells not treated with blebbistatin, as indicated. **A,** Probabilities for markers to vinculin inter-distances <60 nm. **B,** Probabilities for intra-marker distances <60 nm.

Figure 9. Simulated fluorescence images of cell adhesions and corresponding nearest neighbor histograms. A, Simulated randomized distribution of proteins inside and outside of FAs in a cell at 40 nm resolution. **B**, The same image but simulated with 250 nm resolution. **C**, Simulated partially randomized distribution of proteins inside FAs with completely randomized distribution between the FAs. **D**, Simulated completely randomized distribution of proteins in a cell. All images are simulated without any noise, and have a size of 10 X 10 μm^2 with a total number of ~ $2.5 \cdot 10^3$ proteins in each color. **E**, The nearest neighbor histograms of five set of these images were obtained, showing the partially (C) (red filled bars) and completely (A) (blue line) randomized distribution in FAs, as well as completely randomized distribution in the whole cell area analyzed (D) (black line).

Figure 10. Nearest neighbor analysis and STED resolution. A, Probability distribution of the nearest neighbor of talin to self-distances as an example of bipolar distribution. Red filled bars show the distribution for the case inside

individual FAs, and green filled bars for the case outside of FAs, without blebbistatin treatment. The blue empty bars show the nearest neighbor distance distribution in cells after blebbistatin treatment. Median values of nearest neighbor distances for each case are shown in the figure. **B**, Histogram showing the resolution of our system. Point spread functions (PSFs) obtained in each channel by averaging over 10 selected PSFs from the immunofluorescence raw images of targeted proteins. FWHM denotes full width half maxima. FWHM is widely used as indicator for microscopic resolution. Although, it is common practice that one single PSF from an image is chosen to demonstrate the resolution, we used the average from 10 PSFs instead, which is more statistically sound. **C**, The increased resolution of our system is further demonstrated by the paxillin signal in the same are of a cell by the confocal (left panel), raw data STED image (middle panel) and the deconvoluted STED image (right panel).

Figure 11. Working hypothesis. Schematic presentation of the suggested organization of adhesion marker proteins inside, and between FA, as indicated. Loss of contractile force decrease the co-localization between different types of adhesion markers, while it can increase the co-localization between markers of the same type. This is indicated by shorter distances between markers of the same type, than between markers of different types in the image. Taken together, this suggest that a contractile force exerts a non-random control on the localization of proteins within FAs.

Figure 1

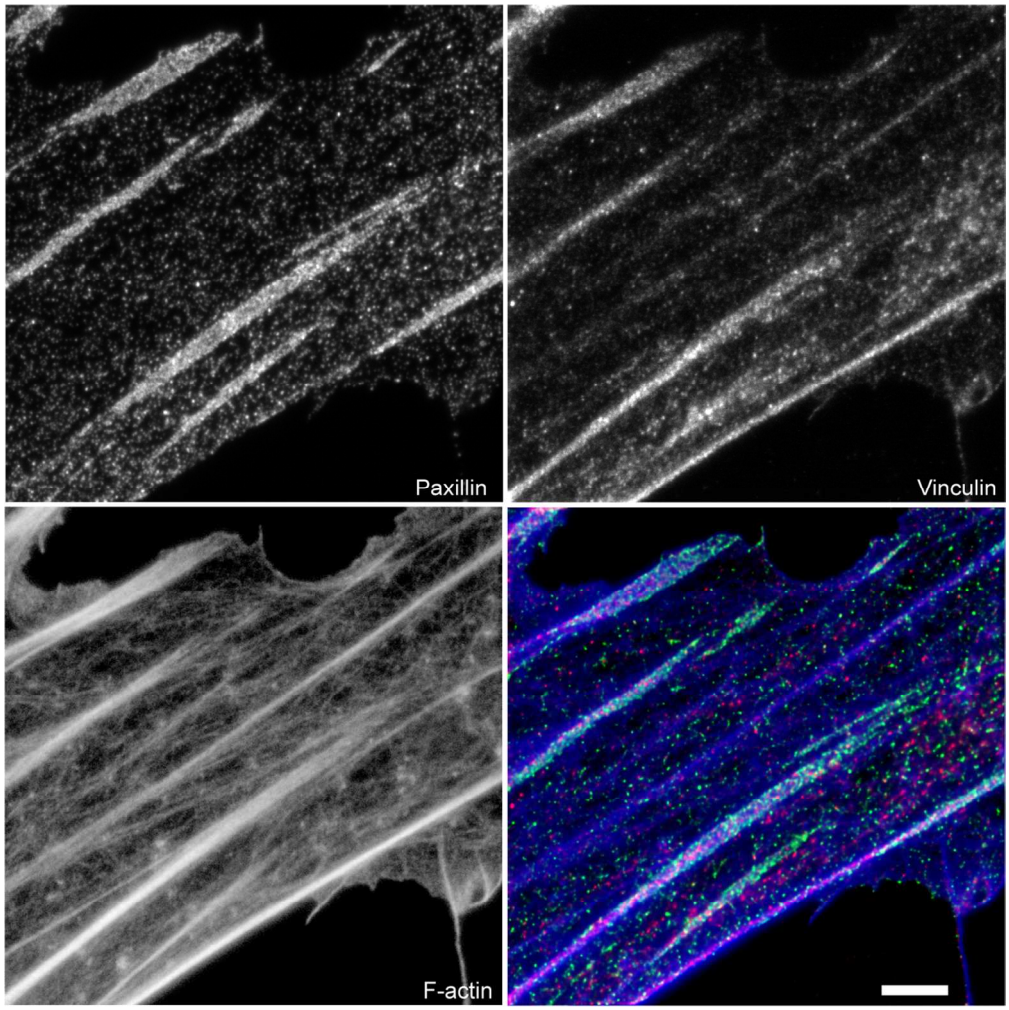

108x112mm (300 x 300 DPI)

Figure 2

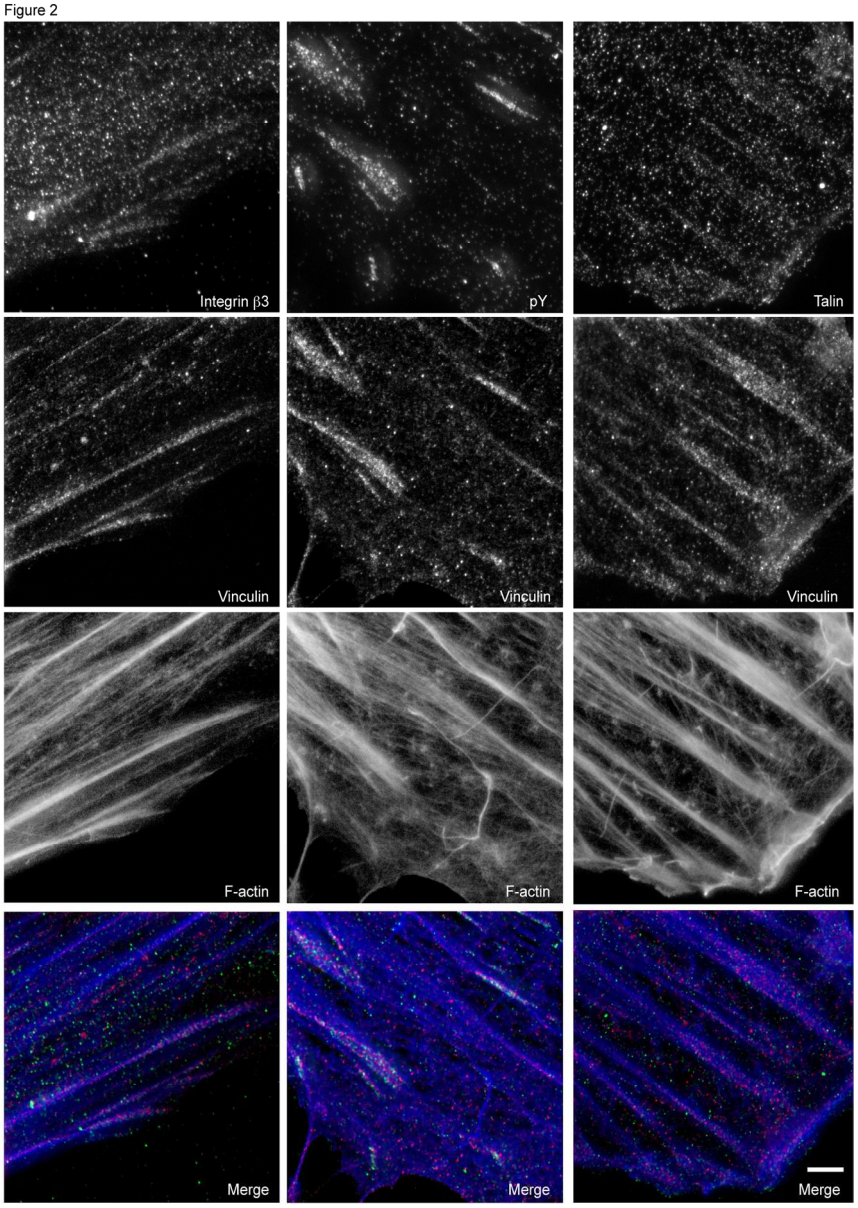

139x191mm (300 x 300 DPI)

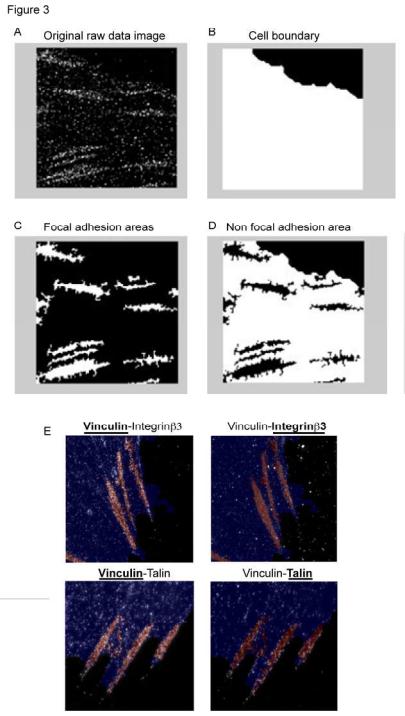

214x212mm (300 x 300 DPI)

Figure 4

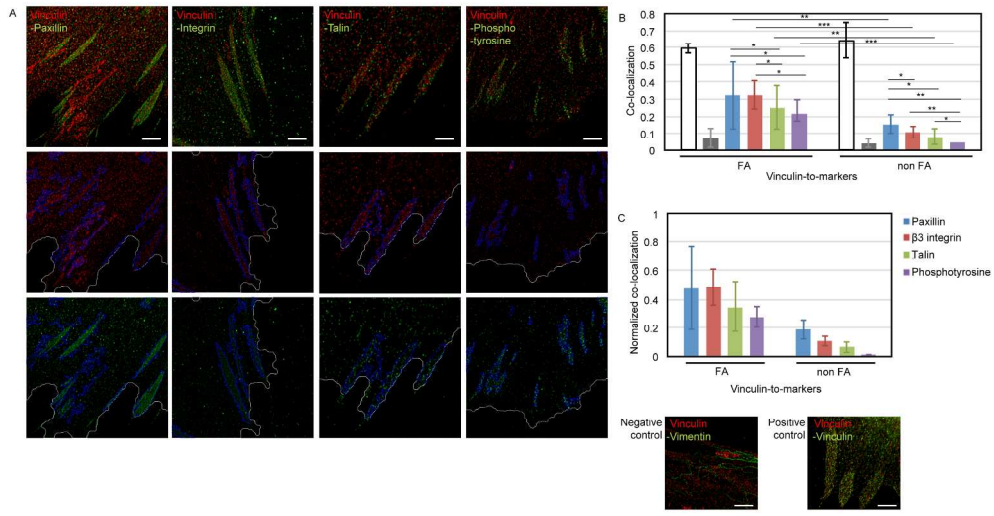

233x152mm (300 x 300 DPI)

Figure 5

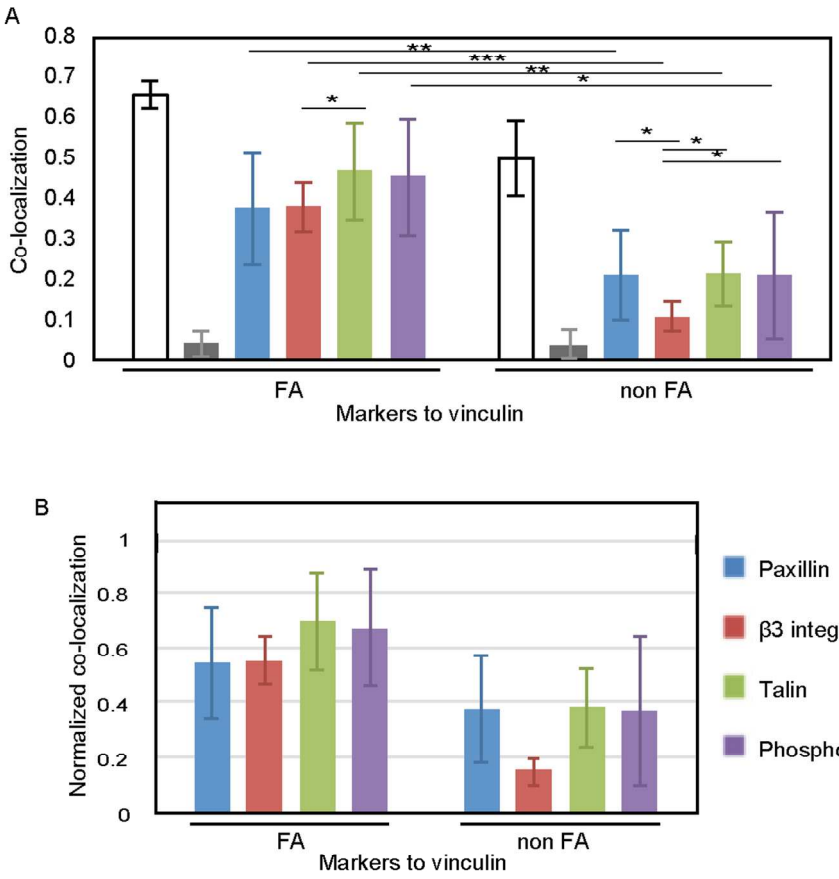

109x109mm (300 x 300 DPI)

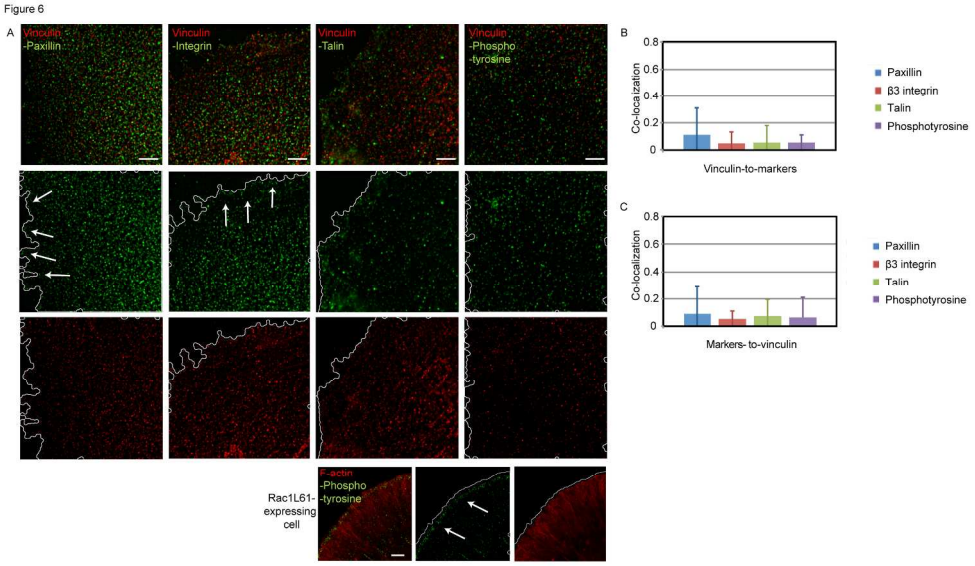

227x129mm (300 x 300 DPI)

Figure 7

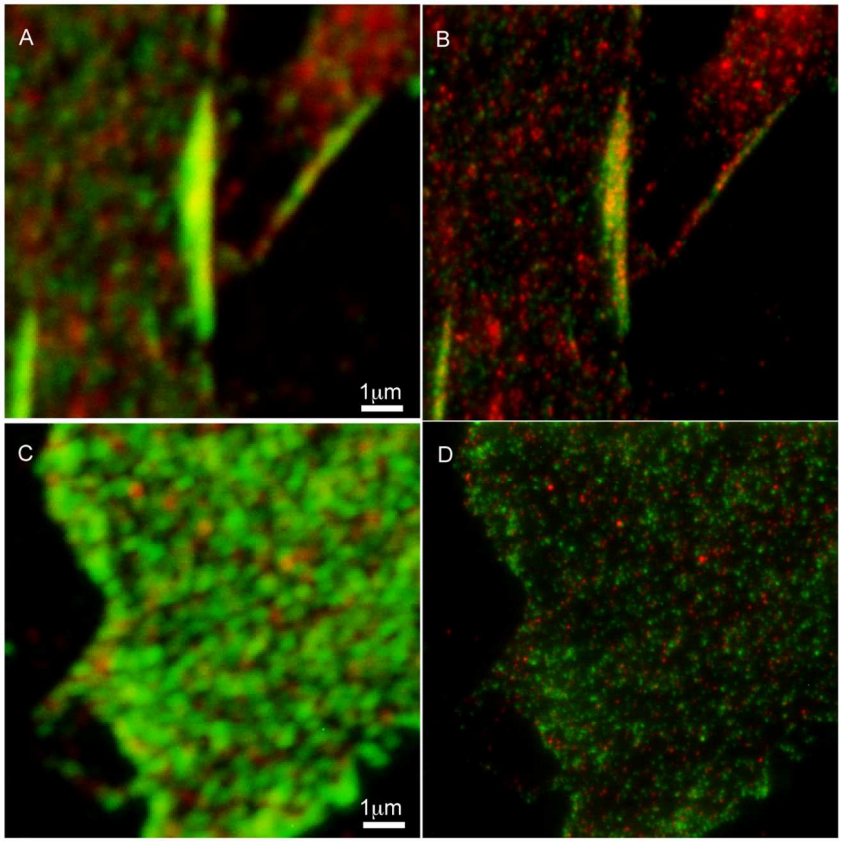

96x135mm (300 x 300 DPI)

Figure 8

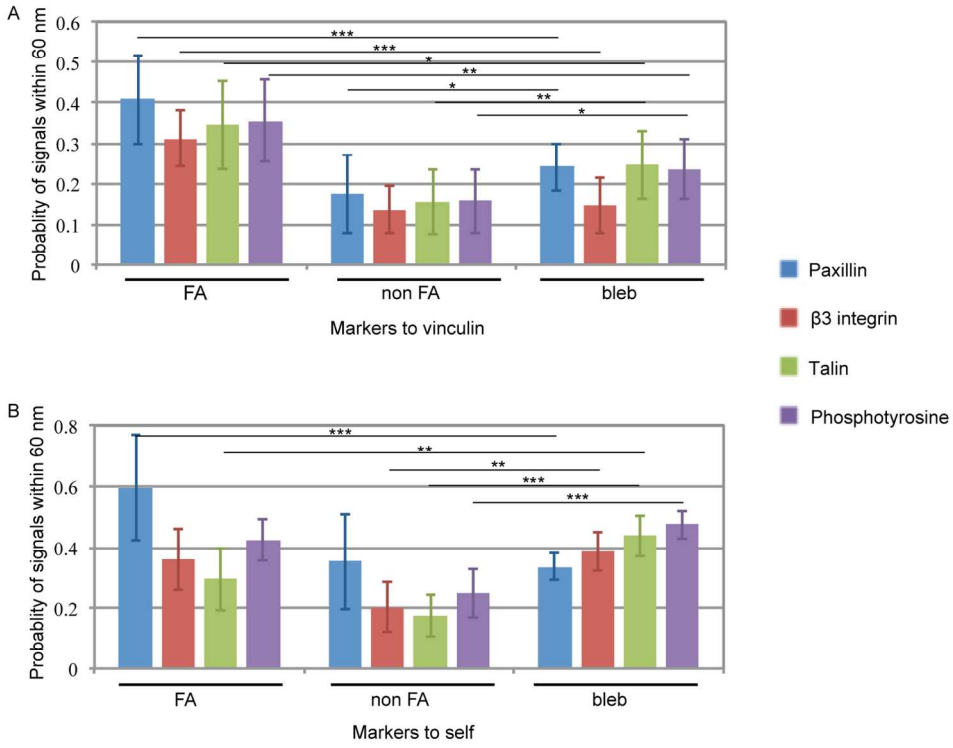

133x104mm (300 x 300 DPI)

Figure 9

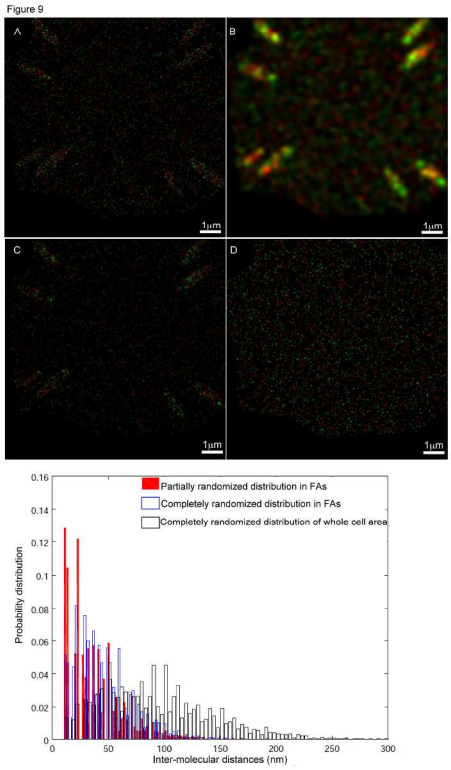

248x267mm (300 x 300 DPI)

Figure 10

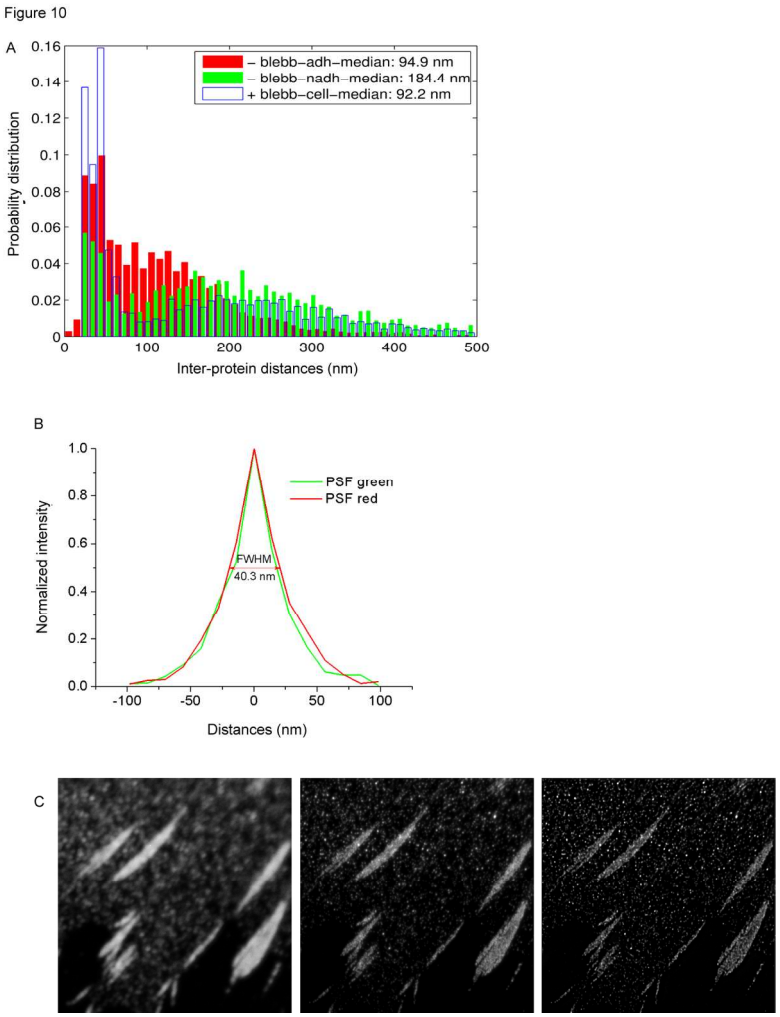

129x199mm (300 x 300 DPI)

Figure 11

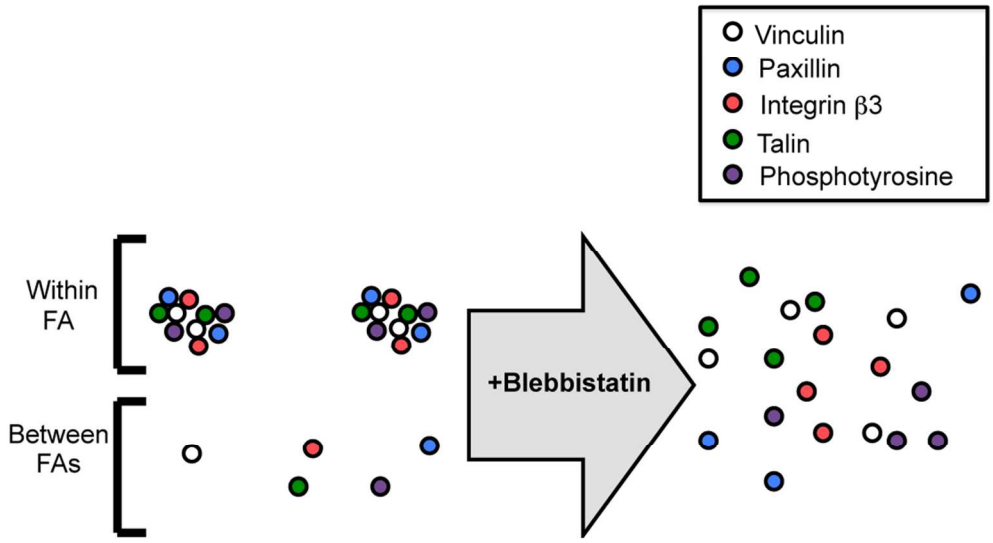

95x55mm (300 x 300 DPI)